Characteristics of the 1998 Summer Monsoon Onset
over the Northern South China Sea

Richard H. JOHNSON and Paul E. CIESIELSKI

Department of Atmospheric Science, Colorado State University, Fort Collins, CO 80523, USA

Abstract

Observations from the May–June 1998 South China Sea Monsoon Experiment (SCSMEX) have been used to determine the characteristics of the onset of the summer monsoon over the northern South China Sea (SCS). The onset occurred in mid-May with a rapid increase in deep convection over a week-to-ten-day period, followed by a ~ten-day break, and then a resumption of deep convection for a week-to-ten-day period in early June. The temporal and spatial variabilities of rainfall rates from the atmospheric moisture budget, satellite, and model estimates generally agree well, although the mean rainfall rate from the models for the 47-day Intensive Observing Period (IOP) is about 25% greater than the other estimates.

The SST gradually increased over the northern SCS during the IOP, interrupted by slight cooling following monsoon onset until early June when the warming resumed. Surface sensible and latent heat fluxes increased after onset, but then decreased in June as a result of warm, moist air advecting over cooler water near the south China coast. The mean apparent heat source Q_1 during convective periods resembled that determined for other tropical oceanic regions with a peak near 400 hPa. The apparent moisture sink Q_2 also resembled profiles for other tropical regions, except for larger values below 900 hPa. The heating and moistening rates and vertical eddy flux of total heat during the early-June active period were greater than those observed during the May monsoon onset active period, indicating more vigorous deep convection as the monsoon ensued, a finding supported by Tropical Rainfall Measuring Mission (TRMM) precipitation radar data.

1. Introduction

The Asian summer monsoon is a major component of the Northern Hemisphere summertime circulation system. The onset of the Asian summer monsoon is concurrent with the reversal of the temperature gradient south of the Tibetan Plateau (Flohn 1957; Yanai et al. 1992; Li and Yanai 1996). The initial onset occurs in early to mid-May over the South China Sea (SCS) area (Tao and Chen 1987). This part of

Corresponding author: Richard H. Johnson, Department of Atmospheric Science, Colorado State University, Fort Collins, CO 80523, USA.
E-mail: johnson@atmos.colostate.edu

the Asian summer monsoon, involving the SCS and surrounding land masses, is referred to as the South East Asia Monsoon or SEAM. In early spring, convection in the SEAM region begins to shift northward from the equator and monsoon rains become anchored over the Borneo-Malaysia-Indo-China land bridge from mid-April until mid-May. Then convection appears to rapidly jump across the SCS during mid-to-late May and establish itself over southern China and the northern SCS (Hirasawa et al. 1995; Lau and Yang 1997; Lau et al. 1998). The subsequent arrival in June of the rains over central China and Japan marks the beginning of the Meiyu and Baiu rainy seasons over those areas, respectively.

During the summer monsoon, the convective areas of southern China and the northern SCS areas provide a significant contribution to the total precipitation and diabatic heat source in the Asian monsoon system (Luo and Yanai 1984; Yanai and Tomita 1998). Several studies of latent heating distributions have been carried out over mainland China. Atmospheric budget studies for the Yangtze Valley show the existence of both convective and stratiform precipitation during the Meiyu, with considerable interannual variability (Luo and Yanai 1984; Kato 1985; Ding and Wang 1988; Ding and Hu 1992). In a study of three summer monsoon seasons, Johnson et al. (1993) found bands of maximum heating and moistening characteristic of deep convection just inland and parallel to the coastline of southern China during the pre-Meiyu and Meiyu rainy periods.

In contrast, very little is known about the part of the monsoon heat source that extends over the northern SCS. Satellite studies (e.g., Lau and Yang 1997) indicate a sudden increase in high cloudiness during onset around mid-May in the northern SCS, although there is considerable year-to-year variability. However, details of these cloud fields and their changes with the onset are not known.

In May-June 1998 the South China Sea Monsoon Experiment (SCSMEX; Lau et al. 2000) was conducted to investigate processes associated with the onset of the SEAM. SCSMEX provides a first opportunity to study the detailed characteristics of convection and circulation changes over the northern SCS during the SEAM onset. Multiple observation platforms (e.g., soundings, Doppler radar, ships, wind profilers, etc.) were deployed during SCSMEX to explore these changes. In this study the primary focus will be on data from the atmospheric sounding network. Specifically, the evolution of large-scale and regional-scale flows, precipitation patterns, and tropospheric heating and moistening will be examined for the 1998 summer monsoon onset using SCSMEX sounding data. Precipitation estimates based on atmospheric budgets will be compared to those obtained from satellite measurements, with particular emphasis on Tropical Rainfall Measuring Mission (TRMM) observations (Kummerow et al. 2000).

2. Data

2.1 Sounding network and quality control procedures

During the May-June 1998 South China Sea Monsoon Experiment (SCSMEX), a sounding network was established in the South China Sea (SCS) and surrounding region to investigate the onset and development of the East Asian monsoon. Preliminary results from the SCSMEX sounding network have been reported in Ding and Liu (2001). The SCSMEX network was contained within the larger domain of the GEWEX Asian Monsoon Experiment (GAME). Sounding sites within the SCSMEX/GAME domain and the May–June 1998 mean sea surface temperature (SST) are shown in Fig. 1. The mean SST field was derived from daily values obtained from the TRMM Microwave Imager (TMI) SST product (Wentz et al. 2000). Figure 1 contains information concerning the vertical resolution and frequency of data re-
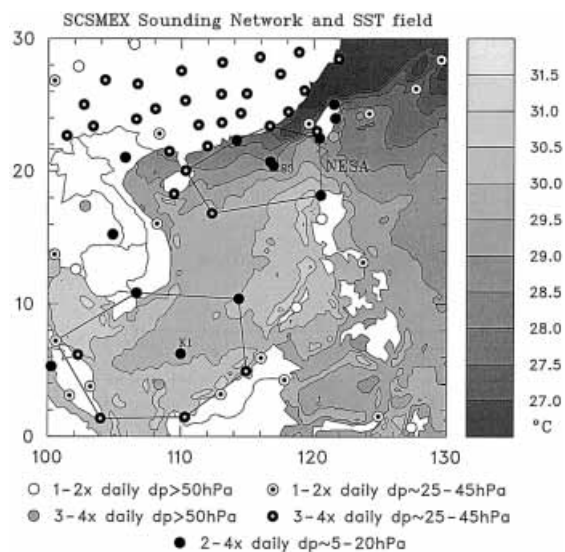

Fig. 1. SCSMEX/GAME sounding network and SST distribution (scale to right) for May–June 1998. Frequency of observations and vertical resolution are indicated by dots with various shadings (*dp* refers to vertical resolution; *S*3 to R/V *Shiyan #3*; *K*1 to R/V *Kexue #1*). Sounding polygons in the northern and southern South China Sea are also indicated; NESA refers to Northern Enhanced Sounding Array.

ceipt for all of the sites during the 47-day Intensive Observing Period (IOP) (5 May–20 June). The highest sounding frequency and resolution were in the vicinity of the SCS (up to 4 launches per day and 5-hPa vertical resolution) decreasing to 1–2 times per day and operational vertical resolution ($\sim$30–100 hPa) away from the SCS. Two special sounding networks are indicated by the polygons in Fig. 1, one in the northern SCS—the Northern Enhanced Sounding Array or NESA—surrounding the dual-Doppler array (the TOGA radar aboard R/V *Shiyan #3* and the BMRC C-POL radar on Dongsha Island) and the other surrounding the R/V *Kexue #1* in the southern SCS—the Southern Enhanced Sounding Array. These networks were designed to determine and contrast the properties of convection in two distinct oceanic regions of the Asian monsoon. However, this study will focus only on results for the NESA.

Figure 1 shows that a strong north-south SST gradient existed across the NESA during SCSMEX. Cooler waters near the south China coast, left over from the winter monsoon, existed throughout the IOP, although the gradient weakened slightly throughout the period. A tongue of cooler water extended over *Shiyan #3*, which reduced the surface fluxes at this location following monsoon onset (to be discussed later).

A variety of sounding systems were used in the SCSMEX/GAME domain ranging from supplemental systems to operational systems, the latter typically differing from one country to the next. At supplemental sites established specifically for SCSMEX—*Shiyan #3*, *Kexue #1*, and Laoag, Philippines (WMO 98223)—Vaisala GPS systems were employed, providing high ($\sim$2 s) vertical resolution data. Elsewhere, a range of sounding types were used consisting mostly of the operational systems of the various countries of the region.

The multiplicity of sounding types presents a problem for quality-control efforts. Biases associated with different sounding systems are not so easy to identify and remove. Some studies have reported biases for observations of height (Collins 2001) and humidity (Soden and Lanzante (1996) from the operational sondes of this region. Recent studies using TOGA COARE (Tropical Ocean Global Atmospheric Coupled Ocean-Atmosphere Response Experiment) data

have shown that the Vaisala sensors typically report relative humidity about 5% too dry in the lower troposphere whereas the VIZ sensors are excessively moist (Zipser and Johnson 1998; Lucas and Zipser 2000). Owing to the variety of humidity biases in the SCSMEX region, spurious humidity gradients can develop which contaminate the moisture budgets. As of yet, corrections have not been incorporated into our budget computations.

Sounding quality control procedures patterned after those used in TOGA COARE (Loehrer et al. 1996) have been applied to the raw SCSMEX/GAME sounding data. This procedure includes automated internal consistency checks (e.g., gross limit and vertical consistency checks) and the assignment of quality flags. In addition, each of the 23,042 soundings from 162 sites was visually inspected up to 100 hPa using skew-T plots for the thermodynamic variables and vertical profiles for the u and v-wind components. Further details and access to quality-controlled datasets are at http://updraft.atmos.colostate.edu/~scsmex/.

2.2 Objective analysis

In this study gridded fields of horizontal wind components u and v, temperature T, specific humidity q, and geopotential height z at 1° resolution over the area covering 80–130°E, 10°S–40°N have been computed from the quality-controlled sounding data using the multiquadric interpolation scheme of Nuss and Titley (1994). Details of the procedure can be found in Johnson and Ciesielski (2000). Owing to the numerous oceanic data-void regions in the large SCSMEX/GAME domain, grid points at 5° intersections having no sounding data within a 3° radius are assigned GAME Reanalysis values (Yamazaki et al. 2000). The impact of this procedure on results for the NESA region is minimal; however, in areas such as the Bay of Bengal and western Pacific, the gridded fields are essentially those of the GAME Reanalysis. Soundings were taken only at 0000 and 1200 UTC at Laoag so those for 0600 and 1800 UTC were constructed by linear interpolation of the 0000 and 1200 UTC data.

The vertical p-velocity ω used in computing the atmospheric budgets was obtained through the kinematic method where horizontal divergence is integrated upward starting at the sur-

face where the condition $\omega = 0$ is imposed.[1] Next, the divergence field is mass balanced in the vertical by assuming adiabatic flow at 100 hPa and using a method suggested by O'Brien (1970) to yield an adjusted divergence (δ^a), where $\delta^a = \delta + \delta^c$, δ is the uncorrected divergence and δ^c is the correction needed to achieve mass balancing. Since budget calculations use both the vertical and horizontal velocities, it is useful to adjust the horizontal wind field to ensure consistency with the corrected divergence profile. Hereafter, references to divergence and horizontal wind will refer to these adjusted values. To do this, we solve $\nabla^2 \chi^c = \delta^c$ with $\chi^c = 0$ on the boundaries from which we obtain a correction to the divergent wind component (χ^c), where ∇^2 is the Laplacian operator on a sphere. This choice of boundary condition on χ^c allows for a particular solution which minimizes (maximizes) the kinetic energy of the divergent (rotational) flow, which in general, is meteorologically reasonable (Sangster 1960).

2.3 Special considerations for topographic effects

Since the sounding data over the SCS are sparse and at some locations along mountainous coastlines, special consideration must be given to topographic effects. In particular, the sounding sites in Taiwan and at Laoag in the Philippines composing the eastern portion of the NESA are in proximity to large mountain barriers (Fig. 2a). The flow at 925 hPa over the northern SCS during the undisturbed pre-onset period of 5–12 May (Fig. 2a) illustrates the impact of these barriers. Specifically, localized blocking of the low-level easterly flow by the 2–3 km mountains to the east of Laoag is aliased onto larger scales by the objective analysis scheme. Very likely, the easterly flow north of Luzon in the Bashi Channel is not as weak as the interpolation scheme depicts in Fig. 2a based on the Laoag and Taiwan soundings. For this pre-onset period the mean low-level flow

---

[1] Computation of topographically forced vertical motion at the lower boundary as in Luo and Yanai (1983) was not carried out because the 1° horizontal grid resolution does not adequately resolve the steep topographic features of Taiwan and Luzon resulting in unrealistic surface vertical velocities in these regions.
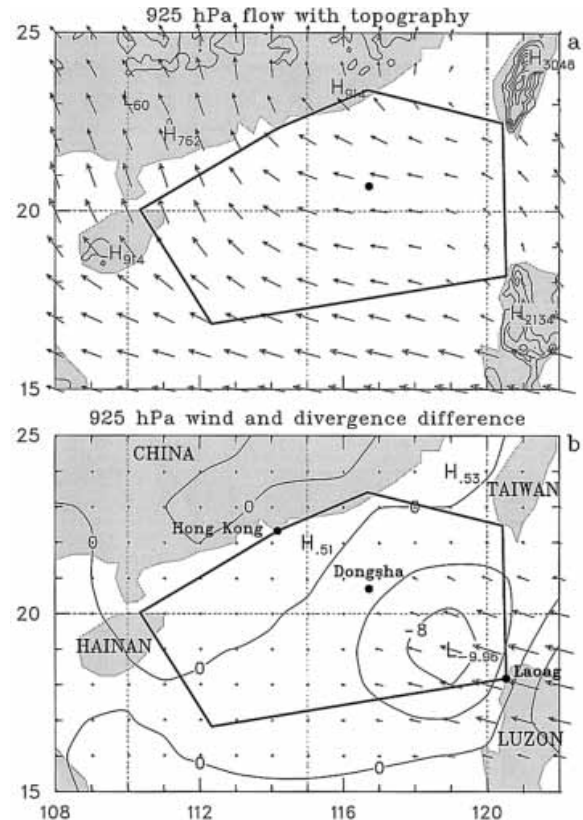

Fig. 2. (a) Average wind vectors for 5–12 May 1998 pre-onset period at 925 hPa from gridded analysis over northern South China Sea using unadjusted Laoag sounding winds. Elevation contours at 500-m intervals. Maximum vector = 7 m s^{-1}. (b) Fields of adjusted 925-hPa winds and divergence minus unadjusted values. Adjusted fields are determined by replacing Laoag winds below 700 hPa with JMA/GAME Reanalysis winds. Replacement removes area of strong divergence downstream of Luzon. Maximum vector = 4 m s^{-1}; divergence units 10^{-6} s^{-1}.

turns to southerly over Taiwan, so effects of blocking on computations for the NESA are not as pronounced. The aliasing near Laoag leads to excessively strong low-level divergence over the northern SCS which, it turn, leads to excessive subsidence and unrealistic negative precipitation rates diagnosed from the moisture budget during this time (shown later). To assess the impact of the blocking, winds below 700 hPa at Laoag are replaced by GAME

Reanalysis winds (at the grid point nearest Laoag) and the resulting difference in winds and divergence at 925 hPa is shown in Fig. 2b. It can be seen that the addition of GAME Reanalysis winds at Laoag increases the strength of the low-level eastsoutheasterly flow over northern Luzon and adds convergence (reduces divergence) over the SCS. This single change has the effect of reducing the diagnosed negative precipitation considerably over the NESA (shown later). The effect of terrain blocking over the NESA is minimal after onset when winds shift to westerly. To lessen the impact of these blocking effects on analyses over the northern SCS, winds below 700 hPa at Laoag (only this site) are replaced with GAME Reanalysis winds for the remainder of the study.

2.4   Other data sources

As described above, GAME Reanalysis data are used to supplement data from the sounding network to fill in voids and lessen the impacts of topography on northern SCS budgets. The GAME reanalysis employs a three-dimensional optimum interpolation scheme and the Japan Meteorological Agency (JMA) forecast model; has T213 (0.5625 degree) horizontal resolution and 30 vertical layers; and uses satellite cloud-drift winds, aircraft reports and wind profiler observations, in addition to the enhanced SCSMEX/GAME sounding network (Yamazaki et al. 2000).

Satellite data are used from several sources: 2.5°-resolution Outgoing Longwave Radiation data from the National Center for Atmospheric Research (NCAR), 1°-resolution daily rainfall values from the TRMM 3B42 combined Precipitation Radar (PR) and TMI rainfall algorithms, and high-resolution TRMM PR data based on the 2A25 algorithm (Kummerow et al. 2000). In addition, 1°-resolution rainfall data are obtained from the Global Precipitation Climatology Project (GPCP; Huffman et al. 2001). Surface rainfall are also obtained from the European Centre for Medium Range Weather Forecasts (ECMWF) 1°-resolution operational analyses. The JMA/GAME Reanalysis was also used to obtain rainfall and surface flux estimates at 1.25° resolution for the NESA.

Surface fluxes from *Shiyan #3* have also been used in our study. These fluxes were obtained by applying the TOGA COARE bulk flux algo-rithm of Fairall et al. (1996) to National Center for Atmospheric Research (NCAR) measurments made aboard *Shiyan #3* (D. Parsons 2001, personal communication). A procedure has been developed similar to that used by Lin and Johnson (1996) to adjust the JMA/GAME Reanalysis fluxes over the northern SCS by the ratio of the ship fluxes to the reanalysis fluxes at a grid point nearest the ship. The adjustment is constrained in such a way that the ratio is always greater than zero. It turns out that after monsoon onset, the ship fluxes were considerably less than model fluxes, such that the averages of the above ratio for latent and sensible heat fluxes are 0.50 and 0.76, respectively. For the period around the end of May and first of June when *Shiyan #3* was off station, these mean values were used to adjust the fluxes.

3.   Large-scale evolution of the flow and convection during onset

The evolution of the flow accompanying the onset of the 1998 summer monsoon has been discussed in detail by Ding and Liu (2001). They noted that the onset occurred first over the northern SCS around 15 May and was influenced significantly by the southward propagation of cold air from midlatitudes, as often occurs (Chang and Chen 1995; Chan et al. 2000). Over the central and southern SCS, the onset occurred slightly later, around 20 May, and was characterized by an eastward retreat of the western Pacific subtropical ridge and the establishment of southwesterlies across the SCS (Ding and Liu 2001). The rapid large-scale circulation changes at 850 and 200 hPa at this time are shown in Fig. 3. From 19 to 21 May the 850-hPa subtropical ridge quickly withdrew from the SCS and from 19 to 22 May the 200-hPa anticyclone center shifted north-ward to near the head of the Bay of Bengal.

Also seen at 200 hPa is the passage of a westward-moving equatorial disturbance over Indonesia and Sumatra. This disturbance has the signature of a mixed Rossby-gravity wave (Matsuno 1966; Yanai and Maruyama 1966). A time series of the meridional wind v at *Kexue #1* (Fig. 4) indicates a prominent shift in the upper-tropospheric winds over the southern SCS reflecting the passage of this wave, with a maximum amplitude in v fluctuation near 150 hPa. Inspection of similar time series of v
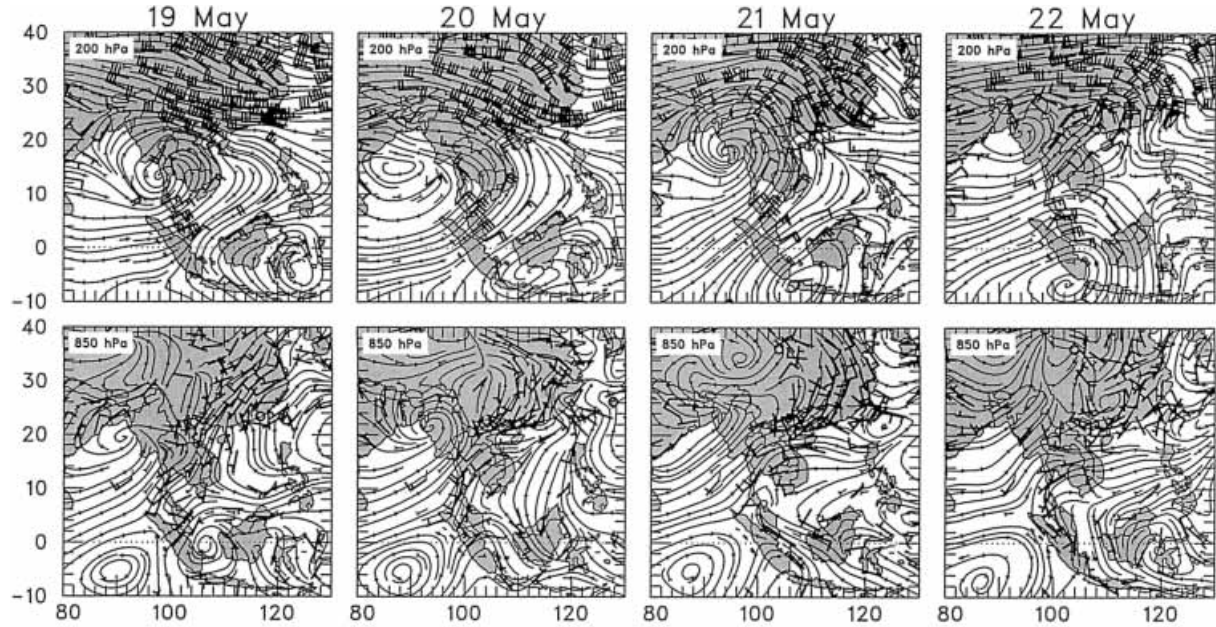
Fig. 3. Streamline analyses at 200 hPa on 19–22 May 1998 (top panels) and at 850 hPa (bottom panels). Wind barbs at the sounding sites are indicated.

from Malaysia indicates that this wave moved westward at $\sim$16 m s^{-1} and had a wavelength of $\sim$5000 km. The meridional winds display a westward tilt with height, associated with an upward wave energy flux (Yanai and Hayashi 1969). Although the origin of this disturbance
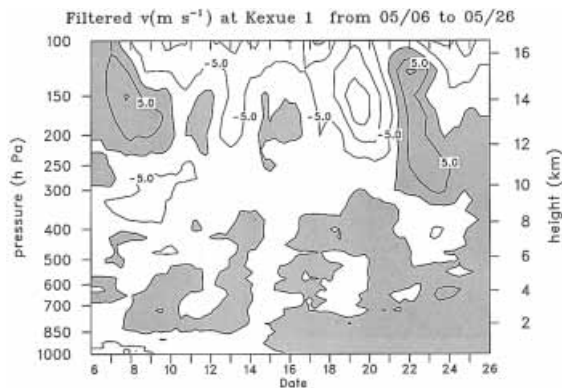

Fig. 4. Time series of filtered (five-point running mean of six-hourly data) meridional wind component v (m s^{-1}) at *Kexue #1* from 00 UTC 6 May to 00 UTC 26 May 1998. Contour interval is 5 m s^{-1} (positive values shaded).

has not been determined, it may be related to lateral forcing by extratropical disturbances (e.g., Magaña and Yanai 1995) since westerlies extended into the deep Tropics on the 19th and earlier (Fig. 3), which would allow the equatorward propagation of midlatitude disturbances through a "westerly duct" (Webster and Holton 1982). Recent studies of equatorially trapped waves indicate that westward-propagating mixed Rossby-gravity waves can exhibit strong vertical coupling as a result of deep convection (Hendon and Liebmann 1991; Wheeler et al. 2000). The flow transitions at upper and lower levels in Figs. 3 and 4, namely, a shift to low-level southerly flow preceding (by several days) a shift to northerly flow near 150 hPa, resemble those described by Wheeler et al. (2000) for vertically coupled mixed Rossby-gravity waves and suggest a possible link between the timing of the monsoon onset in the southern SCS (commencement of low-level southwesterlies) and the occurrence of equatorial waves.

The linkage of the SCS monsoon onset to midlatitude effects can also be seen in Fig. 5, a Hovmöller diagram of OLR and 850-hPa zonal wind component over the longitudes of the

SCS. In early May the low-level flow over the SCS was easterly in association with the subtropical ridge to the north. A clear signal of southward propagation of high cloudiness into the northern SCS can be seen in mid-May and then into the central SCS near 10°N in late May. The onset of westerlies was coincident with the arrival of high cloudiness. In June, both southward and northward propagating bands on convection can be seen, each accompanied by surges in the westerlies (Chang and Chen 1995; Chan et al. 2000). The onset of the SCS monsoon has also been linked to eastward- and westward-propagating disturbances on 30–60 and 12–24 day timescales, respectively (Chen and Chen 1995), but those features cannot be seen in Fig. 5.

4. Atmospheric variability over the northern South China Sea during the SCSMEX IOP

Precipitation over the NESA has been computed from the moisture budget using the gridded dataset following Yanai et al. (1973):
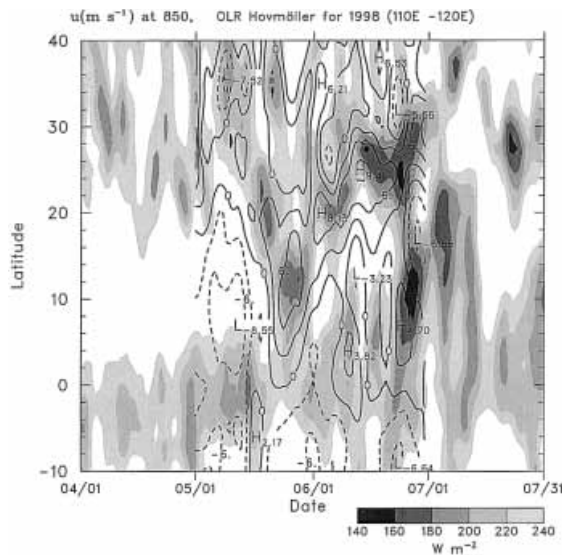
$$\langle Q_2 \rangle = L(P - E), \tag{1}$$

u(m s⁻¹) at 850.   OLR Hovmöller for 1998 (110E -120E)

Fig. 5. Hovmöller diagram of OLR (shaded; scale at lower right) and zonal wind component u (m s^{-1}; westerlies, solid; easterlies, dashed) at 850 hPa between 110 and 120°E (South China Sea). Winds are shown for SCSMEX May and June 1998 periods.

where $Q_2 \equiv -L(\partial \bar{q}/\partial t + \overline{\mathbf{v}} \cdot \nabla \bar{q} + \bar{\omega} \partial \bar{q}/\partial p)$ is the apparent moisture sink, q the specific humidity, L the temperature-dependent latent heat of vaporization, P precipitation rate, E evaporation rate, overbar denotes a horizontal average, $\langle \ \rangle \equiv 1/g \int_{p_T}^{p_s} (\ ) dp$, p_T is the tropopause pressure and p_s the surface pressure. Surface evaporation E over the NESA is based on the GAME reanalysis values adjusted by measurements from *Shiyan #3* as described in Section 2. We also compute the apparent heat source Q_1, defined as $c_p[(\partial \overline{T}/\partial t + \overline{\mathbf{v}} \cdot \nabla \overline{T} + (p/p_0)^\kappa \bar{\omega} \partial \bar{\theta}/\partial p)]$, where $\kappa = R/c_p$, R is the gas constant, and c_p the specific heat at constant pressure for moist air.

In order to view changes over the northern SCS, gridded fields have been averaged over the NESA. Time series of u, v, and relative humidity for May and June over the NESA are shown in Fig. 6. The onset of low-level westerlies in mid-May can be seen to be related to an upper-tropospheric westerly wind maximum, further indicating a connection between the monsoon onset over the northern SCS and midlatitude disturbances (Ding and Liu 2001). Eventually in June, the upper-level westerlies were replaced by easterlies as the 200-hPa anticyclone built northward toward the Tibetan Plateau. Reversals of the low-level and upper-level zonal component of the flow from May to June can be seen in Fig. 7. The meridional winds in Figs. 6 and 7 show that low-level southerlies strengthened during June as the summer monsoon advanced and heavy rains shifted northward toward the Yangtze Valley. Although the relative humidity varied significantly on ~week to ten-day time periods (Fig. 6), the mean profiles for May and June were almost the same (Fig. 7).

Time series of divergence, vertical motion, Q_1, and Q_2 are shown in Fig. 8. Two extended periods of deep convection are inferred, one in mid-May and the other in early June. Strong upward motion, peaking in the mid-to-upper troposphere can be seen at these times. During these periods, peaks in upper-level divergence occurred between 125 and 150 hPa, with a deep layer of convergence in the low-to-midtroposphere. Q_1 and Q_2 displayed maxima characteristic of deep convection: peaks in Q_1 in the mid- to upper troposphere and peaks in Q_2 in the mid- to lower troposphere (Luo and Ya-
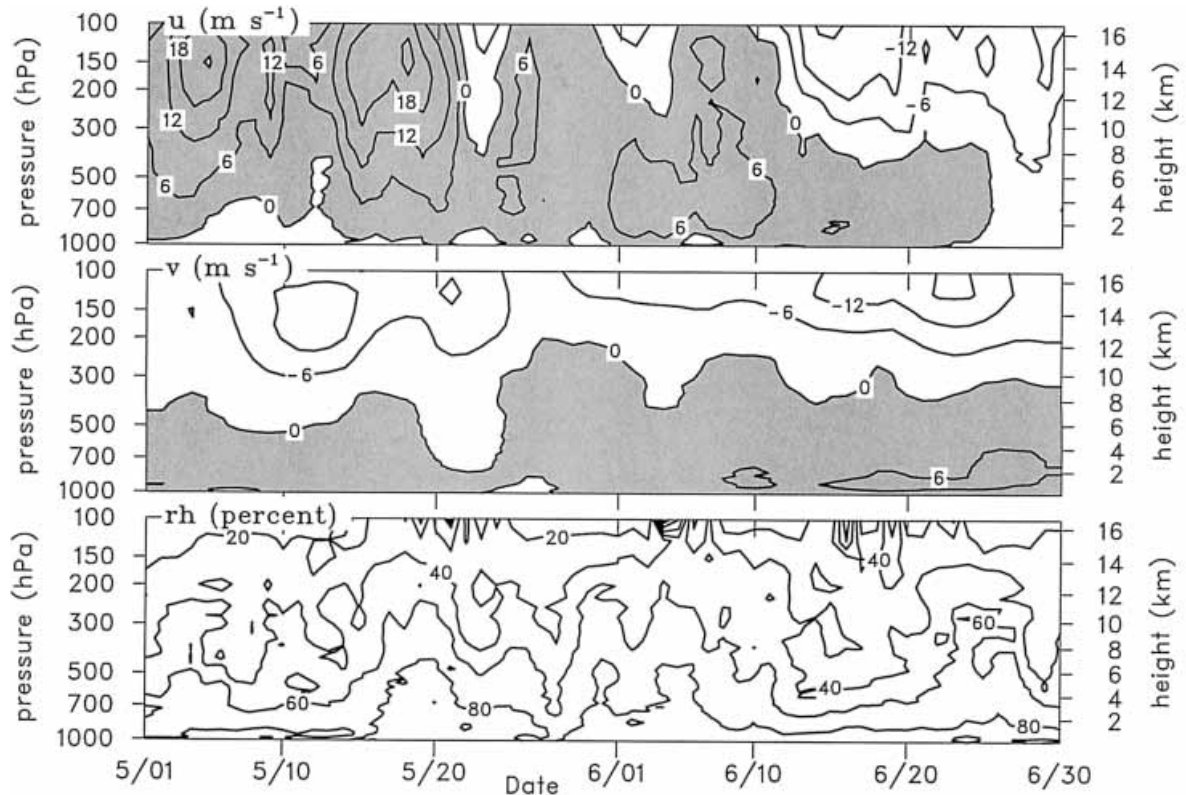
Fig. 6. Time series of u, v and relative humidity over the NESA during May and June 1998. Positive values of wind are shaded.

nai 1984). Strong downward motion was diagnosed prior to the monsoon onset on 15 May, between the two convectively active periods, and again in mid-to-late June. The periods of
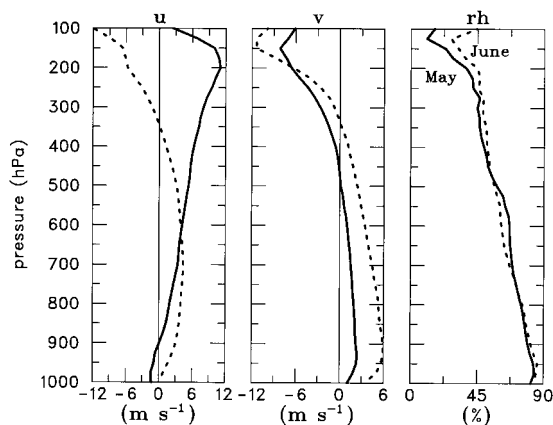

Fig. 7. Vertical profiles of u, v and relative humidity for May (solid) and June (dashed) 1998.

upward and downward motion correspond well to periods of moistening and drying, respectively, in the mid- to upper troposphere (see relative humidity panel in Fig. 6). The dry period over the northern SCS in mid-June marked the first stage of the Meiyu season, when heavy rainfall shifted northward to the region south of the Yangtze Valley (Ding and Liu 2001).

Averages of divergence, vertical motion, Q_1, and Q_2 for the NESA are shown in Fig. 9 for the 37-day period from the monsoon onset on 15 May through 20 June.[2] There is strong low-level convergence, upper-level divergence peaking at 150 hPa, and mid-level convergence. The

2 We suspect errors in the pre-onset period are not totally eliminated by replacement of Laoag winds by GAME Reanalysis winds below 700 hPa (note in Fig. 8 unrealistic values of $Q_1 < -4$ K day^{-1} in the upper troposphere prior to onset in mid-May), so this period of the IOP is excluded from the averages in Fig. 9.
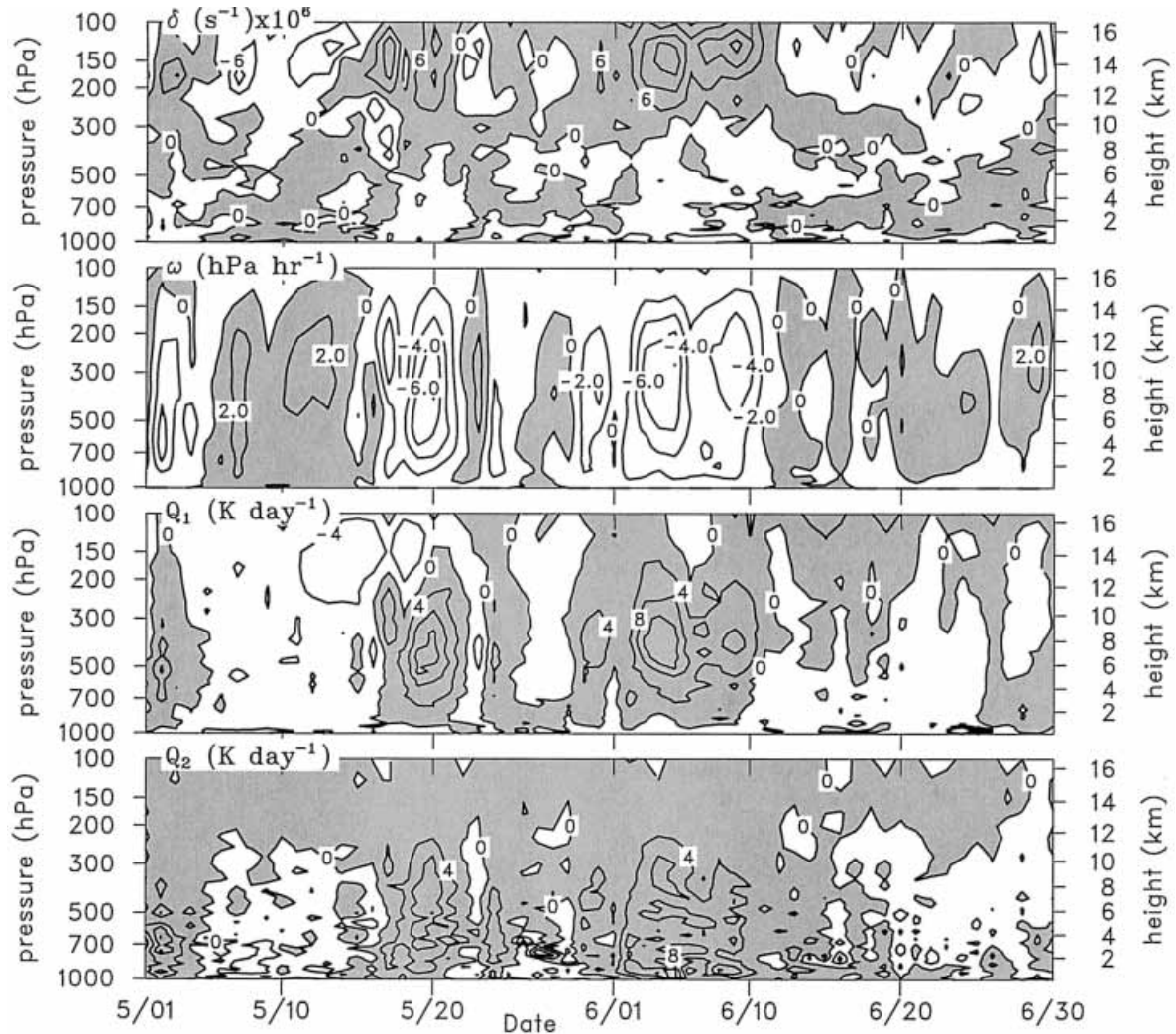
Fig. 8. Time series of divergence, vertical motion, Q_1, and Q_2 over the NESA during May and June 1998. Shaded values are positive.

latter feature may be evidence of "melting-layer convergence" in deep convective systems near the 0°C level arising from extensive regions of stratiform precipitation (Mapes and Houze 1995; Johnson et al. 1996). The mid-level convergence gives rise to an inflection in the ω profile between 600 and 700 hPa, suggesting the upper peak in ω in Fig. 9 may reflect an important contribution from the stratiform components of the convective systems. The mean Q_1 and Q_2 profiles are indicative of deep convection, with the shape of Q_1 resembling that determined for the western Pacific (Yanai et al. 1973) and the eastern Atlantic (Thomp-

son et al. 1979). The negative values of Q_1 near the surface may indicate the effects of rainfall evaporation. The shape of Q_2 also resembles that determined in the above studies, except below 850 hPa. The Q_2 peak between 900 and 950 hPa does not have a counterpart in the other studies. Although it may be related to condensation near cloud base, it is more likely a consequence of errors in the low-level vertical motion over the NESA. Unlike the deep Tropics, horizontal gradients of low-level specific humidity exist in this region (in association with the horizontal gradients of SST, Fig. 1). Horizontal advection of q not properly compen-
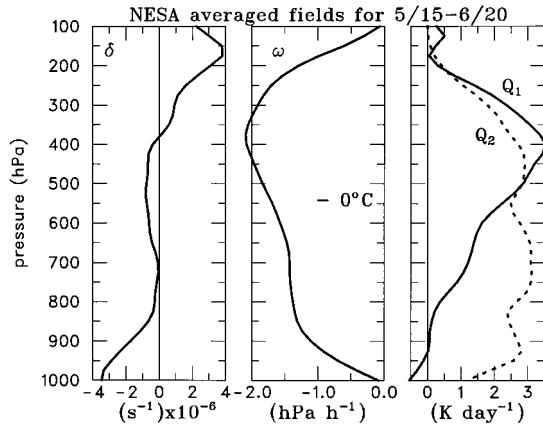
Fig. 9. Vertical profiles of divergence, vertical motion, Q_1, and Q_2 over the NESA from 15 May through 20 June 1998.

Fig. 10. Time series of SST (solid), surface air temperature T_0 (dotted), surface specific humidity q_0 (dashed), CAPE, vertical motion at 400 hPa, and OLR over the NESA for May and June 1998. Shaded times are outside the SCSMEX IOP.

sated by vertical advection of q may yield errors low-level values of Q_2. The low-level distribution of Q_2 could also be partly affected by moisture biases from the various sounding systems of the region which could introduce spurious low-level moisture advection; however, the extent of this effect is not known.

There is an interesting contrast between the heat and moisture budgets for the SCSMEX NESA and those for the western Pacific warm pool. In particular, note that throughout most of the column $Q_2 > Q_1$ (Fig. 9). However, the opposite was found to be true for the warm pool (Johnson and Ciesielski 2000, their Fig. 3). Since

$$\langle Q_R \rangle = \langle Q_1 \rangle - \langle Q_2 \rangle - S - LE, \qquad (2)$$

where $\langle Q_R \rangle$ is the net radiative heating rate, S the surface sensible heat flux, and LE the latent heat flux, this difference implies, assuming that the surface fluxes are comparable, that net tropospheric radiative cooling rate over the SCSMEX region is greater than that over the western Pacific warm pool. Indeed, this is found to be the case, as will be discussed later.

The relationship between SST, surface air temperature T_0, Convective Available Potential Energy (CAPE)[3], vertical motion at 400 hPa,

---

3 CAPE is computed assuming pseudoadiabatic ascent using mean thermodynamic conditions in the lowest 60 hPa, the approximate depth of the mixed layer.
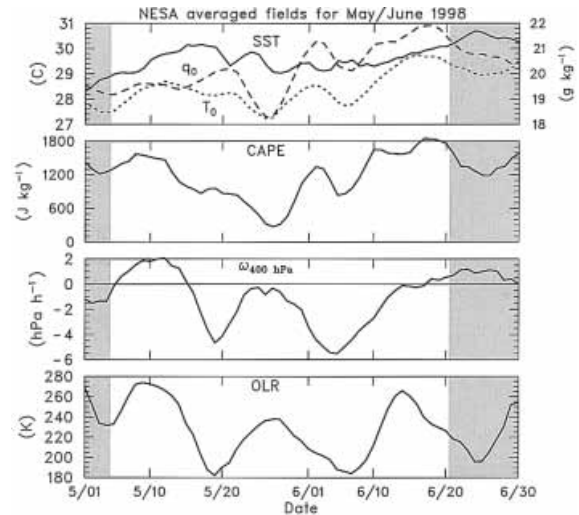
and OLR during May and June over the NESA is shown in Fig. 10. During the IOP, there is a high positive correlation between ω and OLR ($r = 0.81$ for daily-averaged values), indicating the enhanced sounding network is doing a good job of depicting the vertical motion field over the northern SCS. The correlation falls dramatically after the IOP in late June when the enhanced sounding network was terminated. There was a general increase in the SST and surface air temperature throughout the two-month period, interrupted by brief periods of cooling during the late-May and early-June convective episodes presumably due to rainfall, cloud shading, enhanced evaporation, and vertical mixing in the upper ocean. Lau and Yang (1997) show for a ten-year period that the SST over the entire SCS exhibits a broad maximum during May and June, with a gradual cooling thereafter until September. The surface temperature fell during the convective periods, with a corresponding reduction in CAPE, as observed in the eastern Atlantic (Thompson et al. 1979) and elsewhere during deep convection. Further reduction in CAPE occurred after convection abated (around May 25) due to the
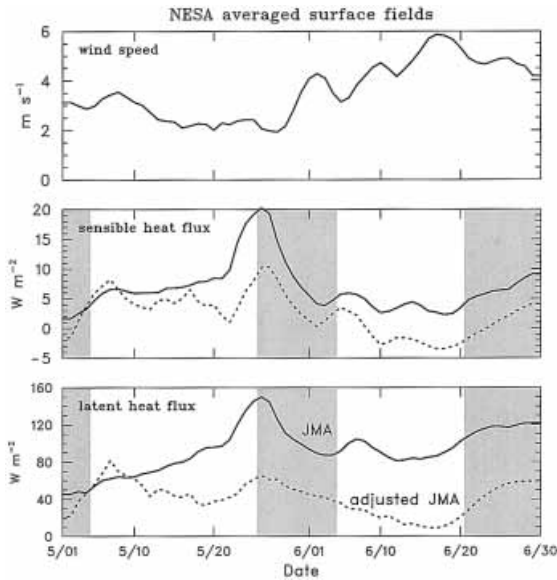
Fig. 11. Time series of wind speed and adjusted (dashed line) and unadjusted (solid line) JMA/GAME Reanalysis sensible and latent heat fluxes. Adjusted fluxes are based on measurements of bulk fluxes from *Shiyan #3* (see text for explanation). Times when *Shiyan #3* was off station are shaded.
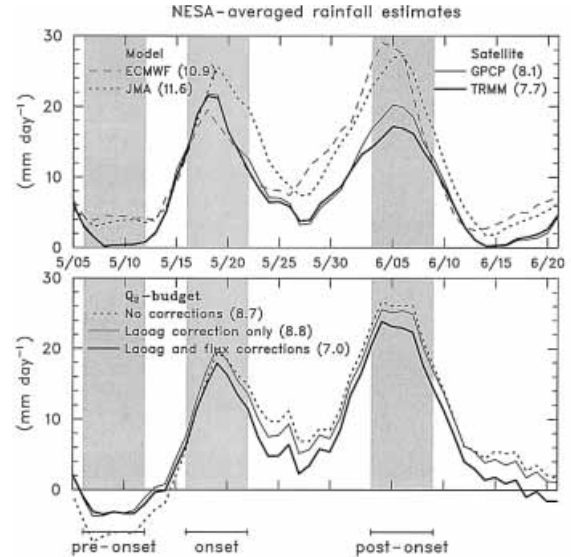

Fig. 12. (top panel) Time series of rainfall rate for model (JMA/GAME Reanalysis, ECMWF) and satellite products (GPCP, TRMM 3B42). (bottom panel) Time series of rainfall rate from moisture (Q_2) budget for three cases: (a) no adjustments to winds at Laoag and surface fluxes, (b) replacement of Laoag winds below 700 hPa by JMA/GAME Reanalysis winds, and, (c) both (b) and adjustment of JMA/GAME surface fluxes by direct measurements at *Shiyan #3*. IOP-mean values are in parentheses. Pre-onset, onset, and post-onset periods are denoted by shading.

passage of a weak cold front from the China mainland. The surface specific humidity, on the other hand, increased during the convective periods. Presumably, dry air from aloft (Fig. 6) was entrained into the mixed layer during the inactive and break periods to reduce the surface specific humidity at those times, although advection of drier air from the mainland could have contributed to the reduction in late May.

The difference between SST and T_0 (Fig. 10) and the time series of wind speed (Fig. 11) indicate that the surface sensible heat flux should exhibit a peak in late May. This result is consistent with the JMA/GAME Reanalysis sensible heat flux time series (Fig. 11) showing a peak in late May. The latent heat fluxes peaked at the same time (Fig. 11), which is consistent with the minimum in q_0 at that time (Fig. 10). The adjusted-JMA fluxes (by the NCAR measurements from *Shiyan #3*) also show a peak in late May, but their amplitudes after the onset of the monsoon are considerably reduced. Direct measurements aboard *Shiyan #3* indicate

markedly reduced surface fluxes after onset. Tentatively, we explain these as a consequence of increased surface southerly flow over the NESA (Figs. 6 and 7) advecting warmer, moister air over colder water (Fig. 1). In fact, the adjusted sensible heat fluxes actually became negative in mid-June as the southerly component of the flow strengthened over the NESA (Fig. 6).

5. Precipitation, heating and moistening rates over the northern South China Sea during active periods of the monsoon

A time series of precipitation rate P from the ECMWF, GAME Reanalysis, GPCP, and TRMM 3B42 datasets is shown in the upper panel of Fig. 12. In the lower panel, the mois-

ture budget results are shown both with and without the replacement of Laoag sounding winds below 700 hPa with GAME Reanalysis winds, and also with both the Laoag wind replacement and using the adjusted JMA/GAME Reanalysis surface fluxes. The large, unrealistic negative precipitation rates in the pre-onset period are reduced considerably by the Laoag replacement, while after onset (when low-level westerlies ensued and terrain-blocking effects over the NESA were less) the differences are generally reduced. When both changes are made, the rainfall rates are reduced throughout most of the period.

Overall, there is good agreement among model, budget, and satellite precipitation time series in Fig. 12. The 47-day mean rainfall rates from the various moisture budget estimates, 6.8–8.6 mm day^{-1}, bracket the GPCP (8.1 mm day^{-1}) and TRMM (7.7 mm day^{-1}) estimates, but average about 25% smaller than the model estimates, 10.9 and 11.6 for the ECMWF and GAME Reanalysis, respectively. The time series indicate two ~10-day rainy periods separated by a break at the end of May. The moisture budget estimates are slightly smaller than the TRMM and GPCP estimates during the first rainy period, and conversely during the second rainy period. We use these time series to define three 7-day periods—pre-onset, onset, and post-onset (Fig. 12)—for further analysis.

Mean profiles of divergence, ω, Q_1, Q_2, and vertical eddy flux of total heat F for these three periods are shown in Fig. 13. Here F is defined by

$$F \equiv -\frac{\overline{h'\omega'}}{g}$$
$$= S + LE + \frac{1}{g}\int_{p_s}^{p}(Q_1 - Q_2 - Q_R)\,dp, \qquad (3)$$

where $h = c_p T + Lq + gz$ is the moist static energy. In computing F, a constant Q_R is assumed (since its vertical profile is not known) so that $F = 0$ at 100 hPa. At the surface, $F = S + LE$, where the surface fluxes from the JMA/GAME Reanalysis have been adjusted by the NCAR-measured fluxes from the *Shiyan #3*. The constant values of Q_R that give $F = 0$ at 100 hPa are −1.6, −1.2, and −1.8 K day^{-1} for the pre-onset, onset, and post-onset periods,

respectively. These cooling rates exceed those of the JMA/GAME Reanalysis (−0.96, −0.20, and −0.16 K day^{-1} for the three successive periods); the GARP Atlantic Tropical Experiment (GATE), −1.1 K day^{-1} from Cox and Griffith (1979); and the western Pacific TOGA COARE estimate of ~−0.5 K day^{-1} (Johnson and Ciesielski 2000). Since there is no clear physical explanation for such large cooling rates, we expect there are still some remaining errors in the budgets for the SCSMEX region. Considering the sensitivity of the budgets over the NESA to low-level winds around Luzon, and the other significant topography surrounding the region (Fig. 2a), it is likely that some of the discrepancy is accounted for by topographic effects. Part may also be due to biases in humidity measurements from the various sounding systems of the region, which may introduce errors in Q_2. Finally, although the sounding data were quality controlled, possible errors (e.g., in the winds) from the operational sites in the region may have eluded detection.

During the undisturbed pre-onset period (Fig. 13), there is upper-level convergence, low-level divergence, and deep subsidence, consistent with the mostly clear skies and high values of OLR (Fig. 10). Radar data from Dongsha Island (20.7°N 116.7°E) during this period indicated no deep convection, with only widely scattered precipitating cumulus congestus clouds (Tom Keenan 2001, personal communication). Q_1 is negative at all levels with values in excess of −2.5 K day^{-1} in the upper troposphere. Since Q_1 approximately equals the net radiative heating rate Q_R during this undisturbed period, we conclude from the large cooling rates that excess subsidence is still being diagnosed at this time despite the adjustment of the low-level winds at Laoag. Q_2 exhibits moistening in the lower troposphere, indicative of shallow nonprecipitating cumulus, but it is also excessive since it extends too high to exclusively represent nonprecipitating clouds.

The profiles of divergence and vertical motion during the May onset and June post-onset periods (Fig. 13) are dramatically different from the pre-onset period. Low-level convergence, upper-level divergence and strong upward motion occur during both periods. Deep convergence extends to 300–500 hPa, similar to that found in the western Pacific (Reed and Recker
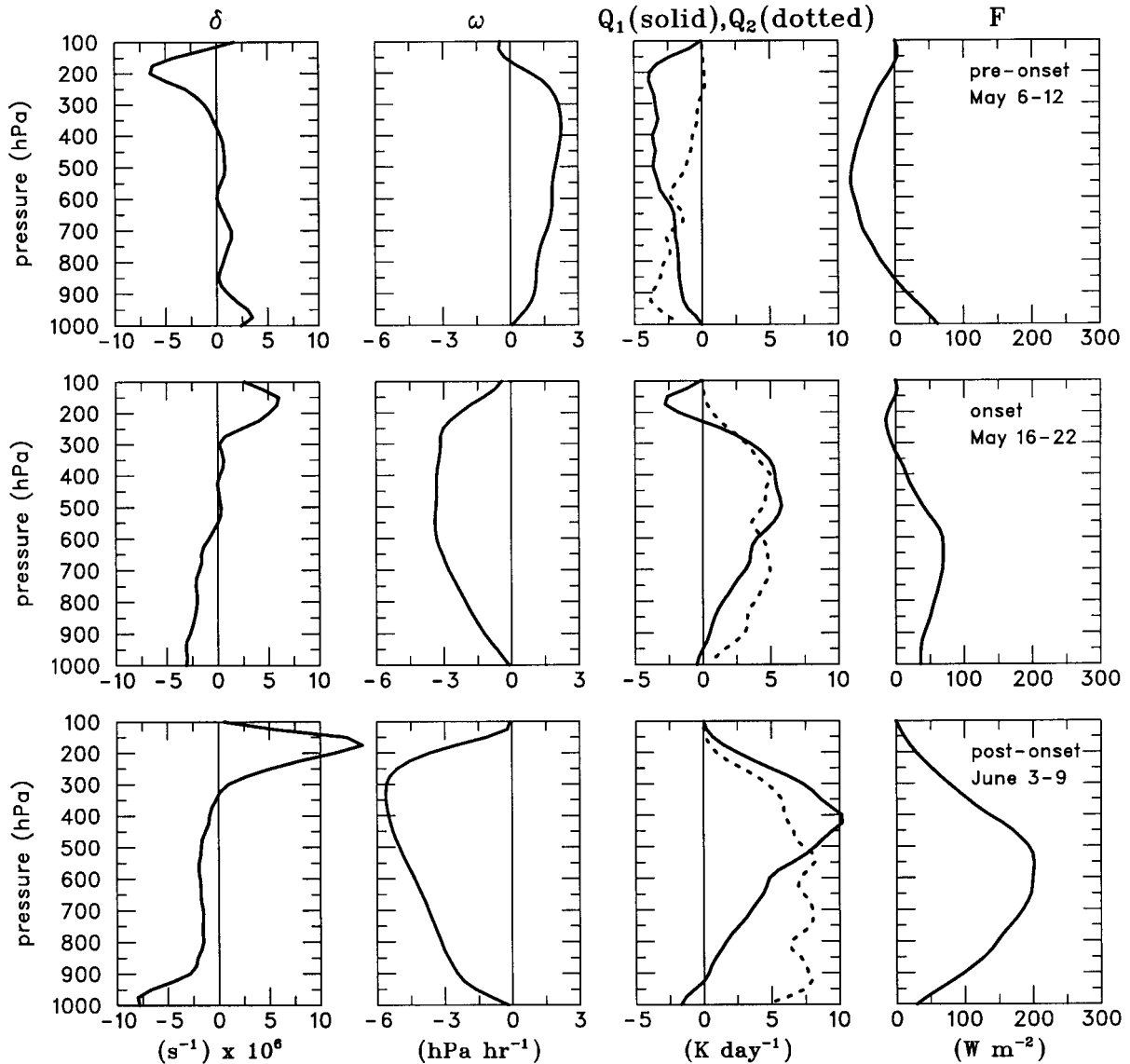
Fig. 13.　Vertical profiles of divergence, vertical motion, Q_1, Q_2, and total energy flux F for the undisturbed pre-onset period (top panel), the onset convective period (middle panel), and the post-onset convective period (bottom panel).

1971; Yanai et al. 1973). Some of this convergence is presumably associated with downdrafts and some with melting-induced convergence in the stratiform precipitation regions (Mapes and Houze 1995). The Q_1 and Q_2 profiles are characteristic of deep convection during the onset and post-onset periods, with a greater separation of the two curves in the post-onset period, suggesting more vigorous deep convection at that time. This conclusion

is supported by profiles of F (Fig. 13), which indicate much stronger eddy heat fluxes during the second active period. The occurrence of more intense convection during the second active period is consistent with higher surface specific humidity q_0 at that time, which also led to slightly higher CAPEs (Fig. 10).

More vigorous convection during the post-onset period is also consistent with TRMM precipitation radar (PR) reflectivity profiles for the
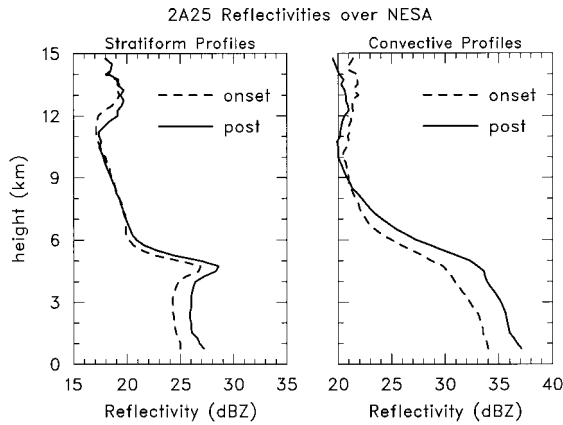
Fig. 14. Vertical profiles of stratiform and convective radar reflectivity from TRMM precipitation radar (PR) using algorithm 2A25 (Kummerow et al. 2000) for onset (16–22 May 1998) and post-onset (3–9 June 1998) periods.

two periods derived from the 2A25 algorithm (Kummerow et al. 2000). Mean reflectivity profiles for stratiform and convective precipitation for thirteen overpasses in each of the periods are shown in Fig. 14. Although the number of overpasses is limited and uncertainties in TRMM-based, weekly mean reflectivity profiles are large (Steiner and Houze 1998), there are over 70,000 individual profiles comprising each of the means. For the times of the overpasses, the budget and PR rainfall rates for the onset period are 11.9 and 11.9 mm day^{-1}, and for the post-onset period are 19.4 and 24.7 mm day^{-1}, respectively. Higher reflectivities are observed in both the stratiform and convective profiles for the post-onset period, supporting the budget findings of stronger convection at that time.

The horizontal distributions of rainfall from the moisture budget, GPCP, TRMM 3B42 combined algorithm, and the JMA/GAME Reanalysis for the onset and post-onset periods are shown in Figs. 15 and 16. For the onset
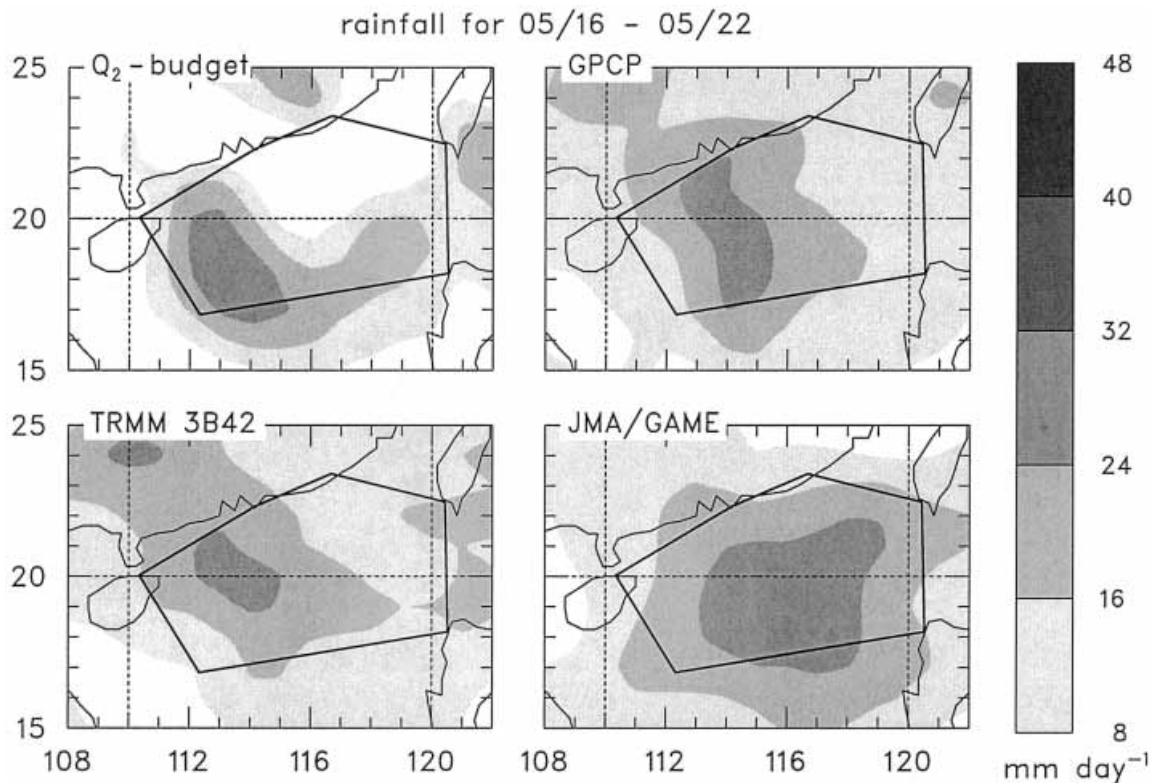

Fig. 15. Horizontal distributions of rainfall rates (scale on right) for the 16–22 May 1998 onset period from the moisture budget, the GPCP, the TRMM 3B42 algorithm, and the JMA/GAME Reanalysis.
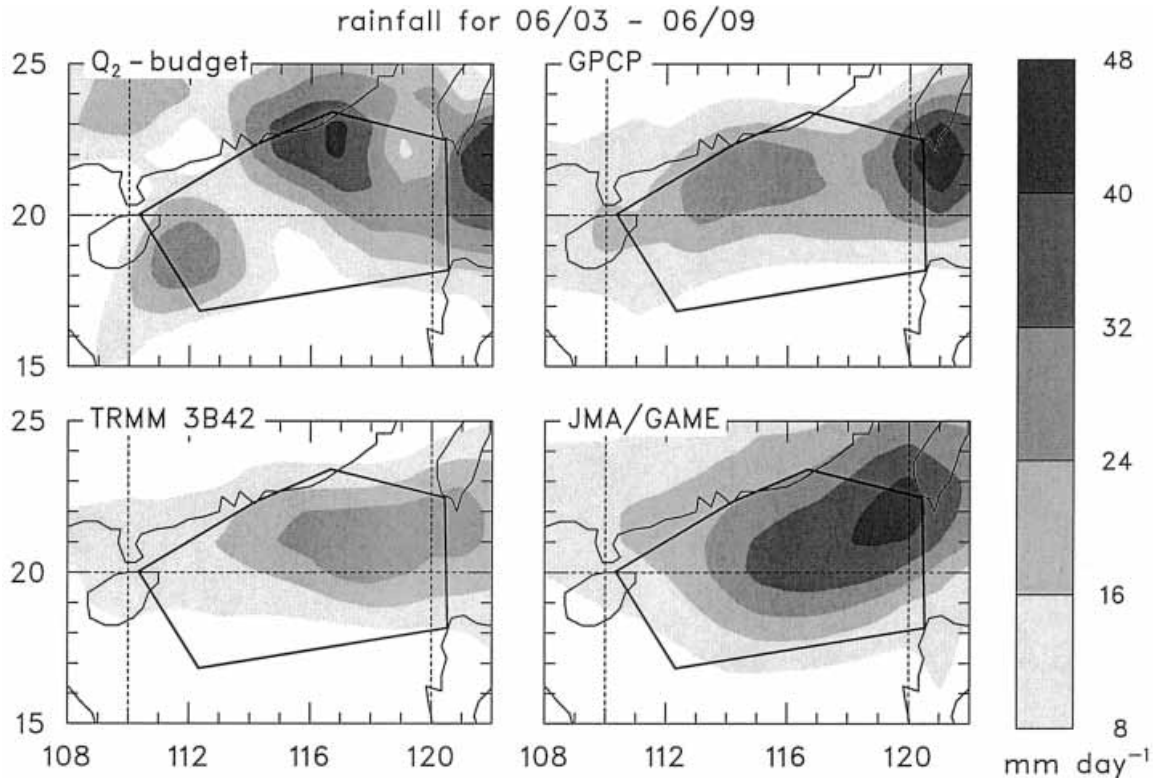
Fig. 16.   Horizontal distributions of rainfall rates (scale on right) for the 3–9 June 1998 onset period from the moisture budget, the GPCP, the TRMM 3B42 algorithm, and the JMA/GAME Reanalysis.

period (Fig. 15) the rainfall amounts and patterns from the budget, GPCP and TRMM are in reasonably good agreement, with greatest amounts in the western half of the NESA. The JMA/GAME Reanalysis does not agree as well with the other two, showing a broad rainfall maximum in the southcentral part of the NESA. The positioning of the primary rainfall maximum away from the south China coastline in the onset period (Fig. 15) may be related to the SST gradient across the region (Fig. 1), i.e., warmer water to the south.

For the post-onset period (Fig. 16) the agreement between the budget, GPCP, and TRMM 3B42 rainfall patterns is also reasonably good with multiple maxima present within and near the NESA. Both the budget and GPCP show two primary maxima, one south of Taiwan and another along the south coast of China (although the positions of the latter differ). The positions of a weaker maximum near Hainan also differ somewhat. The TRMM 3B42 and

JMA/GAME show a single elongated maximum, although their positions generally coincide with the envelope of the strongest maxima for the budget and GPCP.

The generally good agreement between the independent budget, GPCP, and TRMM rainfall patterns for both convectively active periods lends confidence to the ability of the sounding network to describe the heating and moistening distributions reasonably well during SCSMEX. However, integral constraints applied to the budgets that yield estimates for $\langle Q_R \rangle$ indicate that some systematic errors still exist, likely due to topographic effects and biases in the sounding data.

6.   Summary and conclusions

The characteristics of convection over the northern South China Sea (SCS) have been investigated using data from the May–June 1998 South China Sea Monsoon Experiment (SCSMEX). Owing to the sparse sounding net-

work and placement of some sounding sites near elevated terrain, significant topographic effects on the low-level flow were detected over the northern SCS. In particular, during the pre-onset period, the low-level easterly flow at Laoag on Luzon in the northern Philippines was blocked and the effects of this blocking were aliased onto larger scales by the objective analysis scheme. To reduce these effects, winds below 700 hPa at the sounding site at Laoag were replaced by winds from the JMA/GAME Reanalysis, which incorporates other information on the low-level flow over this area (e.g., cloud-drift winds).

The main results from this study are as follows:

- The onset of the monsoon over the northern SCS occurred on 15 May in association with a southward-propagating area of convection from China. At the same time there was a rapid retreat of the western Pacific subtropical high and the passage of a prominent equatorial mixed Rossby-gravity wave over the longitudes of east Asia. The onset was followed by a week-to-ten-day period of deep convection, a ~ten-day break period, and then another week-to-ten-day convectively active period in early June.
- SST gradually increased over the northern SCS during the IOP, interrupted by slight cooling following monsoon onset and during the early-June convective period. Surface sensible and latent heat fluxes increased just after monsoon onset, while CAPE decreased as a result of vertical mixing by deep convection and brief incursions of cool air from the China mainland. Surface fluxes then decreased in June as a result of warm, moist air advecting over cooler water near the south China coast.
- The mean apparent heat source Q_1 during convective periods resembled that determined for other tropical oceanic regions with a peak near 400 hPa. The apparent moisture sink Q_2, also resembled profiles for other tropical regions, except for larger values below 900 hPa. However, the latter feature may be associated with errors in the low-level vertical motion field and/or errors in the humidity field over this data-sparse and topographically influenced region. The budgets indicate

an IOP-mean net tropospheric radiative heating rate of ~ -1.5 K day^{-1}. This cooling rate is larger than other tropical estimates by at least 0.5 K day^{-1}, suggesting that some errors in the budgets still remain (e.g., due to topographic effects, moisture biases at the sounding sites, other errors in the sounding data, sparse sounding network).
- The temporal and spatial variabilities of rainfall rates throughout the SCSMEX IOP from independent estimates—moisture budget and satellites (TRMM and GPCP)—agree well. Agreement with models (GAME Reanalysis and ECMWF operational analysis) is not quite as good in terms of spatial patterns and intensity (the models' mean rainfall rate for the 47-day Intensive Observing Period (IOP) is about 25% greater than the other estimates).
- The heating and moistening rates and vertical eddy flux of total heat during the early-June active period were greater than those observed during the May monsoon onset active period, indicating more vigorous deep convection at that time. This finding is supported by vertical reflectivity profiles from the TRMM precipitation radar.

The generally good agreement between the spatial and temporal variability of rainfall rates determined from the moisture budget and independent satellite estimates lends confidence to conclusions regarding the character of the convective systems inferred from the budget results. However, further work is needed to (1) determine the full effects of topography on the budgets, (2) remove any moisture and other biases from the soundings of the region, and (3) compare budget results with analyses of radar data from the Bureau of Meteorology CPOL radar and the Tropical Ocean Global Atmosphere radar.

An important aspect of the convection in this region not addressed in this paper is its diurnal cycle. Both satellite and radar observations during the experiment clearly indicated a strong diurnal cycle of convection over the northern SCS apparently linked to land and sea breezes along the southern coast of China. Further work is also underway to investigate this aspect of monsoon convection during SCSMEX.

References

Chan, J.C.L., Y. Wang, and J. Xu, 2000: Dynamic and thermodynamic characteristics associated with the onset of the 1998 South China Sea summer monsoon. *J. Meteor. Soc. Japan*, **78**, 367–380.

Chang, C.-P. and G.T.-J. Chen, 1995: Tropical circulations associated with Southwest Monsoon onset and westerly surges over the South China Sea. *Mon. Wea. Rev.*, **123**, 3254–3267.

Chen, T.-C. and J.-M. Chen, 1995: An observational study of the South China Sea monsoon during the 1979 summer. *Mon. Wea. Rev.*, **123**, 2295–2318.

Collins, W.G., 2001: The operational complex quality control of radiosonde heights and temperatures at the National Centers for Environmental Prediction. Part II: Examples of error diagnosis and correction from operational use. *J. Appl. Meteor.*, **40**, 152–168.

Cox, S.K. and K.T. Griffith, 1979: Estimates of radiative divergence during Phase III of the GARP Atlantic Tropical Experiment: Part II. Analysis of Phase III results. *J. Atmos. Sci.*, **36**, 586–601.

Ding, Y.-H. and J. Hu, 1988: The variation of the heat sources in East Asia in the early summer of 1984 and their effects on the large-scale circulation in East Asia. *Advances in Atmos. Sci.*, **6**, 171–180.

—— and X.-F. Wang, 1988: An analysis of the distribution of apparent heat sources and sinks over the middle reaches of Yangtze River during the Meiyu season in 1983. *Tropical Meteorology*, **4**, 134–145 (in Chinese).

—— and Y. Liu, 2001: Onset and evolution of the summer monsoon over the South China Sea during SCSMEX field experiment in 1998. *J. Meteor. Soc. Japan*, **79**, 255–276.

Fairall, C.W., E.F. Bradley, D.P. Rogers, J.B. Edson, and G.S. Young, 1996: Bulk paramaterization of air-sea fluxes for TOGA COARE. *J. Geophys. Res.*, **101**, No. C2, 3747–3764.

Flohn, H., 1957: Large-scale aspects of the "summer monsoon" in South and East Asia. *J. Meteor. Soc. Japan*, **75th Ann. Vol.**, 180–186.

Hendon, H.H. and B. Liebmann, 1991: The structure and annual variation of antisymmetric fluctuations of tropical convection and their association with Rossby-gravity waves. *J. Atmos. Sci.*, **48**, 2127–2140.

Hirasawa, H., K. Kato, and T. Takeda, 1995: Abrupt change in the characteristics of the cloud zone in subtropical East Asia around the middle of May. *J. Meteor. Soc. Japan*, **73**, 221–239.

Huffman, G.J., R.F. Adler, M.M. Morrissey, D.T. Bolvin, S. Curtis, R. Joyce, B. McGavock, and J. Susskind, 2001: Global precipitation at one-degree daily resolution from multisatellite observations. *J. Hydrometeor.*, **2**, 36–50.

Johnson, R.H. and P.E. Ciesielski, 2000: Rainfall and radiative heating rate estimates from TOGA-COARE atmospheric budgets. *J. Atmos. Sci.*, **57**, 1497–1514.

——, Z. Wang, and J.F. Bresch, 1993: Heat and moisture budgets over China during the early summer monsoon. *J. Meteor. Soc. Japan*, **71**, 137–152.

——, P.E. Ciesielski, and K.A. Hart, 1996: Tropical inversions near the 0°C level. *J. Atmos. Sci.*, **53**, 1838–1855.

Kato, K., 1985: On the abrupt change in the structure of the Baiu front over the China continent in late May of 1979. *J. Meteor. Soc. Japan*, **63**, 20–36.

Kummerow, C. and Co-Authors, 2000: The status of the Tropical Rainfall Measuring Mission (TRMM) after two years in orbit. *J. Appl. Meteor.*, **39**, 1965–1982.

Lau, K.-M. and S. Yang, 1997: Climatology and interannual variability of the Southeast Asian Summer Monsoon. *Adv. in Atmos. Sci.*, **14**, 141–162.

Lau, K.-M., H.-T. Wu, and S. Yang, 1998: Hydrologic processes associated with the first transition of the Asian Summer Monsoon: A pilot satellite study. *Bull. Amer. Meteor. Soc.*, **79**, 1871–1882.

—— and Coauthors, 2000: A report of the field operations and early results of the South China Sea Monsoon Experiment (SCSMEX). *Bull. Amer. Meteor. Soc.*, **81**, 1261–1270.

Li, C. and M. Yanai, 1996: The onset and interannual variability of the Asian summer monsoon in relation to land-sea thermal contrast. *J. Climate*, **9**, 358–375.

Lin, X. and R.H. Johnson, 1996: Heating, moistening and rainfall over the western Pacific warm pool during TOGA COARE. *J. Atmos. Sci.*, **53**, 3367–3383.

Loehrer, S.M., T.A. Edmands, and J.A. Moore, 1996: TOGA COARE upper-air sounding data ar-

chive: development and quality control procedures. *Bull. Amer. Meteor. Soc.*, **77**, 2651–2671.

Lucas, C. and E.J. Zipser, 2000: Environmental variability during TOGA COARE. *J. Atmos. Sci.*, **57**, 2333–2350.

Luo, H. and M. Yanai, 1983: The large-scale circulation and heat sources over the Tibetan Plateau and surrounding areas during the early summer of 1979. Part I: Precipitation and kinematic analyses. *Mon. Wea. Rev.*, **111**, 922–944.

——— and ———, 1984: The large-scale circulation and heat sources over the Tibetan Plateau and surrounding areas during the early summer of 1979. Part II: Heat and moisture budgets. *Mon. Wea. Rev.*, **112**, 966–989.

Magaña, V. and M. Yanai, 1995: Mixed Rossby-gravity waves triggered by lateral forcing. *J. Atmos. Sci.*, **52**, 1473–1486.

Mapes, B.E. and R.A. Houze, Jr., 1995: Diabatic divergence profiles in western Pacific mesoscale convective systems. *J. Atmos. Sci.*, **52**, 1807–1828.

Matsuno, T., 1966: Quasi-geostrophic motions in the equatorial area. *J. Meteor. Soc. Japan*, **44**, 25–43.

Nuss, W.A. and D.W. Titley, 1994: Use of multiquadric interpolation for meteorological objective analysis. *Mon. Wea. Rev.*, **122**, 1611–1631.

O'Brien, J.J., 1970: Alternative solutions to the classical vertical velocity problem. *J. Appl. Meteor.*, **9**, 197–203.

Reed, R.J. and E.E. Recker, 1971: Structure and properties of synoptic-scale wave disturbances in the equatorial western Pacific. *J. Atmos. Sci.*, **28**, 1117–1133.

Sangster, W.E., 1960: A method of representing the horizontal pressure force without reduction of station pressures to sea level. *J. Meteor.*, **17**, 166–176.

Steiner, M. and R.A. Houze, Jr., 1998: Sensitivity of monthly three-dimensional radar-echo characteristics to sampling frequency. *J. Meteor. Soc. Japan*, **76**, 73–95.

Tao, S.Y. and L.X. Chen, 1987: A review of recent research on the east Asian summer monsoon in China. *Monsoon Meteorology III*, C.-P. Chang and T.N. Krishnamurti, eds., Oxford University Press, 60–92.

Thompson, R.M., Jr., S.W. Payne, E.E. Recker, and R.J. Reed, 1979: Structure and properties of synoptic-scale wave disturbances in the intertropical convergence zone of the eastern Atlantic. *J. Atmos. Sci.*, **36**, 53–72.

Webster, P.J. and J.R. Holton, 1982: Cross-equatorial response to middle-latitude forcing in a zonally varying basic state. *J. Atmos. Sci.*, **39**, 722–733.

Wentz, F.J., C. Gentemann, D. Smith, and D. Chelton, 2000: Satellite measurements of sea surface temperature through clouds. *Science*, **288**, 847–850.

Wheeler, M., G.N. Kiladis, and P.J. Webster, 2000: Large-scale dynamical fields associated with convectively coupled equatorial waves. *J. Atmos. Sci.*, **57**, 613–640.

Yamazaki, N., H. Kamahor, A. Yatagai, K. Takahashi, H. Ueda, K. Aonashi, K. Kuma, Y. Takeuchi, H. Tada, Y. Fukutomi, H. Igarashi, H. Fujinami, and Y. Kajikawa, 2000: On the release of GAME Reanalysis products, *Tenki*, **47**, 659–663 (in Japanese).

Yanai, M. and T. Maruyama, 1966: Stratospheric wave disturbances propagating ove the equatorial Pacific. *J. Meteor. Soc. Japan*, **44**, 291–294.

——— and Y. Hayashi, 1969: Large-scale equatorial waves penetrating from the upper troposphere into the lower stratosphere. *J. Meteor. Soc. Japan*, **47**, 167–182.

——— and T. Tomita, 1998: Seasonal and interannual variability of atmospheric heat sources and moisture sinks determined from NCEP-NCAR reanalysis. *J. Climate*, **11**, 463–482.

———, S. Esbensen, and J.H. Chu, 1973: Determination of bulk properties of tropical cloud clusters from large-scale heat and moisture budgets. *J. Atmos. Sci.*, **30**, 611–627.

———, C. Li, and Z. Song, 1992: Seasonal heating of the Tibetan Plateau and its effects on the evolution of the Asian summer monsoon. *J. Meteor. Soc. Japan*, **70**, 319–351.

Zipser, E.J. and R.H. Johnson, 1998: Systematic errors in radiosonde humidities: A global problem? *Preprints, 10th Symposium on Meteorological Observations and Instrumentation*, Amer. Meteor. Soc., Phoenix, 72–73.